journal

J. Am. Ceram. Soc., 94 [S1] S204–S214 (2011)
DOI: 10.1111/j.1551-2916.2011.04516.x

A Constitutive Description of the Inelastic Response of Ceramics

Vikram S. Deshpande†

Department of Engineering, University of Cambridge, Cambridge CB2 1PZ, U.K.

E. A. Nell Gamble, Brett G. Compton, Robert M. McMeeking, Anthony G. Evans, and Frank W. Zok

Materials Department, University of California, Santa Barbara, 93106 California

The objective of the article is to present a unified model for the dynamic mechanical response of ceramics under compressive stress states. The model incorporates three principal deformation mechanisms: (i) lattice plasticity due to dislocation glide or twinning; (ii) microcrack extension; and (iii) granular flow of densely packed comminuted particles. In addition to analytical descriptions of each mechanism, prescriptions are provided for their implementation into a finite element code as well as schemes for mechanism transitions. The utility of the code in addressing issues pertaining to deep penetration is demonstrated through a series of calculations of dynamic cavity expansion in an infinite medium. The results reveal two limiting behavioral regimes, dictated largely by the ratio of the cavity pressure p to the material yield strength σ_Y. At low values of p/σ_Y, cavity expansion occurs by lattice plasticity and hence its rate diminishes with increasing σ_Y. In contrast, at high values, expansion occurs by microcracking followed by granular plasticity and is therefore independent of σ_Y. In the intermediate regime, the cavity expansion rate is governed by the interplay between microcracking and lattice plasticity. That is, when lattice plasticity is activated ahead of the expanding cavity, the stress triaxiality decreases (toward more negative values) which, in turn, reduces the propensity for microcracking and the rate of granular flow. The implications for penetration resistance to high-velocity projectiles are discussed. Finally, the constitutive model is used to simulate the quasi-static and dynamic indentation response of a typical engineering ceramic (alumina) and the results compared to experimental measurements. Some of the pertinent observations are shown to be captured by the present model whereas others require alternative approaches (such as those based on fracture mechanics) for complete characterization.

I. Introduction

Ceramics have been used extensively for armor protection. When confined within a metallic medium, their exceptional dynamic strength in compression causes impacting projectiles to deform and erode. Absent the confinement, the tensile stresses induced in the ceramic cause extensive cracking that eliminates the benefit. The practical challenge is to conceive designs that maintain the confinement for a sufficient duration to realize the full benefit. Current design practice has been developed through extensive testing but has limited scope given the large design space; the most efficient approach would incorporate numerical simulations.

Various computational tools have been developed and dynamic constitutive models devised that characterize the response of ceramics to extreme loads.[1–6] In general, two approaches have been used:

(i) Phenomenological damage mechanics, wherein the ceramic is regarded as an elastic–plastic material subject to a notional damage process that reduces the strength as the deformation proceeds.

(ii) Micromechanically motivated models that incorporate aspects of the physics governing compressive damage and plastic deformation.

Each of these approaches has its benefits and draw-backs. The micromechanical models give insight into the mechanisms at play but are computationally too expensive to be used in large-scale structural simulations. On the other hand, while the phenomenological approaches are suited to large-scale computations, they require extensive calibration and typically have a regime of applicability that is limited to scenarios resembling the calibration schemes. Among the phenomenological models, the one that is most complete is that devised by Johnson and Holmquist.[5] The model incorporates a phenomenological law inspired by the response of ceramics impacted at high velocity under highly confined conditions. It embodies a Drucker–Prager yield surface[7] that evolves with damage through the effective plastic strain (analogous to that in the Johnson–Cook model[8] for metals). The representation has multiple coefficients and exponents that require calibration through dynamic measurements. It does not incorporate any microstructural characteristics (such as grain size) or normative material properties (such as toughness and hardness). Nevertheless, when a material has been calibrated in accordance with the proposed protocol, projectile penetration can be simulated with adequate fidelity.[9] The evident limitation is that, for each candidate ceramic, the coefficients and exponents must be recalibrated, because they are not connected to basic microstructure/property relationships.

Recently, Deshpande and Evans[10] (subsequently referred to as DE) devised a micromechanically motivated model that is amenable to large-scale dynamic structural computations. Two specific inelastic phenomena have been included in this model. The first is lattice plasticity due to dislocations and twins, characterized by the von Mises stress relative to the (rate-dependent) flow strength of the material. This property can be probed using hardness measurements conducted with a spherical indenter. The second is damage in the form of microcracks that emanate from preexisting flaws. They evolve subject to a combination of local deviatoric and hydrostatic stresses. The microcracks have dimensions and separations that scale with the grain size. They extend in a manner dictated by the short crack toughness of the ceramic. The constitutive law embodying these mechanisms has been used to successfully simulate the influence of normative material properties, including grain size, hardness, and toughness, on the extents of plastic deformation and damage that occur in polycrystalline alumina upon impact of a hard spherical projectile[11] and upon quasi-static penetration by a hard sphere.[12] The limitation of the foregoing representation is that

A. Heuer—contributing editor

Manuscript No. 28828. Received October 27, 2010; approved February 19, 2011.
This work is financially supported by the Office of Naval Research through a Multidisciplinary University Research Initiative Program on "Cellular Materials Concepts for Force Protection," Prime Award No. N00014-07-1-0764.
†Author to whom correspondence should be addressed. e-mail: vsd@eng.cam.ac.uk

the mechanical response beyond the point at which the damage becomes saturated (namely, the microcracks have coalesced) has yet to be addressed. The present article establishes an approach for representing the behavior of a damage-saturated ceramic and combines with the foregoing lattice plasticity and damage models to produce a unified model that can be used to simulate deep penetration.

The fully comminuted ceramic created within the highly confined environment beneath an impacting projectile is in a unique state. It consists of grain-sized particles bounded by narrow separations between them (Fig. 1) and has a relative density very close to unity because the volume occupied by the separations is small. This state differs from that found in particulate materials such as soils and in powder compacts, which have relative densities around 60%. When subjected to a combination of compressive and shear stress, the particles can slide and rotate past one another: a phenomenon hereafter referred to as *granular plasticity*.

The article is organized as follows: it begins with a description of the unified model, its physical interpretation, and the associated constitutive law. Thereafter, preliminary features of the constitutive response are elucidated via the predicted stress/strain response of a prototypical hard ceramic (namely alumina) under varying levels of stress triaxiality. Subsequently, two specific loading scenarios are examined and, where possible, used to interpret phenomena found experimentally. The first is the expansion of a spherical cavity in an infinite medium. The objective is to characterize the development and propagation of elastic, plastic, and damage waves as well as understand the interplay between plasticity and damage. The second considers quasi-static and dynamic penetration. Here comparisons are made of the predictions of the original DE model and the current constitutive law, with emphasis on the damage evolution pattern and the load versus displacement response.

II. Development of the Constitutive Model

The inelastic deformation of ceramic polycrystals occurs in accordance with the foregoing three primary mechanisms (Fig. 1) proceeding partially in series and partially in parallel. We envisage the ceramic with a population of preexisting flaws or heterogeneities that, under stress, can extend into microcracks. Before microcracks form, plastic deformation can only occur by dislocation slip or twinning: termed *lattice plasticity*. Its onset is characterized by the von Mises yield criterion, depicted in effective stress (σ_e)–mean stress (σ_m) space as a horizontal line (Fig. 2). When microcracks grow and coalesce, the ceramic transitions into a granular medium comprising narrowly separated granules with dimensions dictated typically by the grain size. The fully comminuted ceramic has a small shear yield strength governed by friction between the particles. Its yield criterion has a form similar to Drucker–Prager for granular media. The transition between these two yield surfaces with increasing microcrack density is depicted in Fig. 2. At each level of damage, D, yield is characterized by a sloping line in $\sigma_e-\sigma_m$ space; as described below, we shall assume that all of these lines intercept the lattice plasticity line at the same location. Upon full comminution, inelastic deformation can occur by one of two mechanisms: granular plasticity of the comminuted particles or lattice plasticity within the particles themselves.

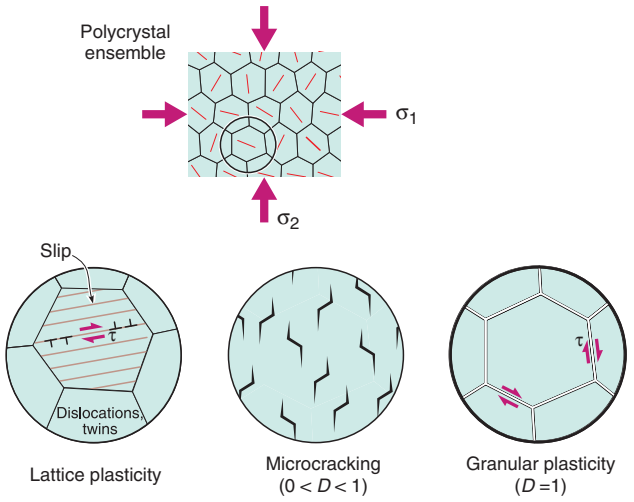

Fig. 1. The inelastic mechanisms included in the constitutive model for ceramics.

To devise a mechanism-inspired model from the foregoing physical picture, the following four elements must be incorporated:

(i) A lattice plasticity model.

(ii) A criterion for the evolution of damage due to microcracking.

(iii) The transition between the yield surfaces for lattice and granular plasticity.

(iv) The incorporation of elasticity (with lattice and granular plasticity) to give the overall constitutive description.

(1) The Constituent Models

(A) Lattice Plasticity: In structural ceramics, lattice plasticity occurs in accordance with two limits: at low strain rates, resistance from the lattice governed by the Peierls stress and, at high rates, phonon drag.[13] With this in mind, we approximate the effective plastic strain rate $\dot{\varepsilon}_e^{pl}$ versus the von Mises effective stress σ_e relationship by

$$\frac{\dot{\varepsilon}_e^{pl}}{\dot{\varepsilon}_0}=\begin{cases}\left(\dfrac{\dot{\varepsilon}_0}{\dot{\varepsilon}_t}\right)^{(1-n)/n}\left(\dfrac{2\sigma_e}{\sigma_0}-1\right) & 2\sigma_e > \sigma_0\left[\left(\dfrac{\dot{\varepsilon}_t}{\dot{\varepsilon}_0}\right)^{1/n}+1\right]\\ \left(\dfrac{2\sigma_e}{\sigma_0}-1\right)^{n} & \sigma_0 < 2\sigma_e \le \sigma_0\left[\left(\dfrac{\dot{\varepsilon}_t}{\dot{\varepsilon}_0}\right)^{1/n}+1\right]\\ 0 & 2\sigma_e \le \sigma_0\end{cases} \tag{1}$$

where $\sigma_0(\varepsilon_e^{pl})$ is the flow stress at an equivalent plastic strain ε_e^{pl}, while $\dot{\varepsilon}_0$ and n are the reference strain rate and strain rate sensitivity exponent, respectively, and $\dot{\varepsilon}_t$ is the transition strain-rate above which plasticity becomes phonon drag limited. Note that the exponent n sets the strain rate sensitivity of the ceramic in the low strain rate regime. Strain hardening is characterized by a conventional power law, notably:

$$\sigma_0=\frac{\sigma_Y}{2}\left[1+(\varepsilon_e^{pl}/\varepsilon_Y)^M\right] \tag{2}$$

where σ_Y is the uniaxial yield strength, ε_Y the plastic strain at which $\sigma_0=\sigma_Y$, and M the strain hardening exponent. Associated flow is assumed with a flow potential, $G_p\equiv\sigma_e$. The plastic strain rate is then

$$\dot{\varepsilon}_{ij}^{pl}=\dot{\varepsilon}_e^{pl}\frac{\partial G_p}{\partial\sigma_{ij}} \tag{3}$$

(B) Microcrack Evolution: The model envisages an array of f microcracks per unit volume, subject to principal stresses σ_1 and σ_3 and growing in an otherwise elastic medium (Fig. 3). Each microcrack develops from an initial flaw, radius a, by means of two wings, length ℓ, extending parallel to X_1 (Fig. 3). The inclined flaws are subject to Coulomb friction, with friction coefficient μ. The radius and separation of the flaws scale with the grain size as $a=g_1d$ and $1/f^{1/3}=g_2d$, respectively, where g_1 and g_2 are parameters. The initial and current levels of damage are expressed respectively as $D_0=(4/3)\pi(\alpha a)^3f$ and $D=(4/3)\pi(l+\alpha a)^3f$, where $\alpha\equiv\tan\psi$ is a shape factor to account for the angle of the initial flaw as shown in Fig. 3. The

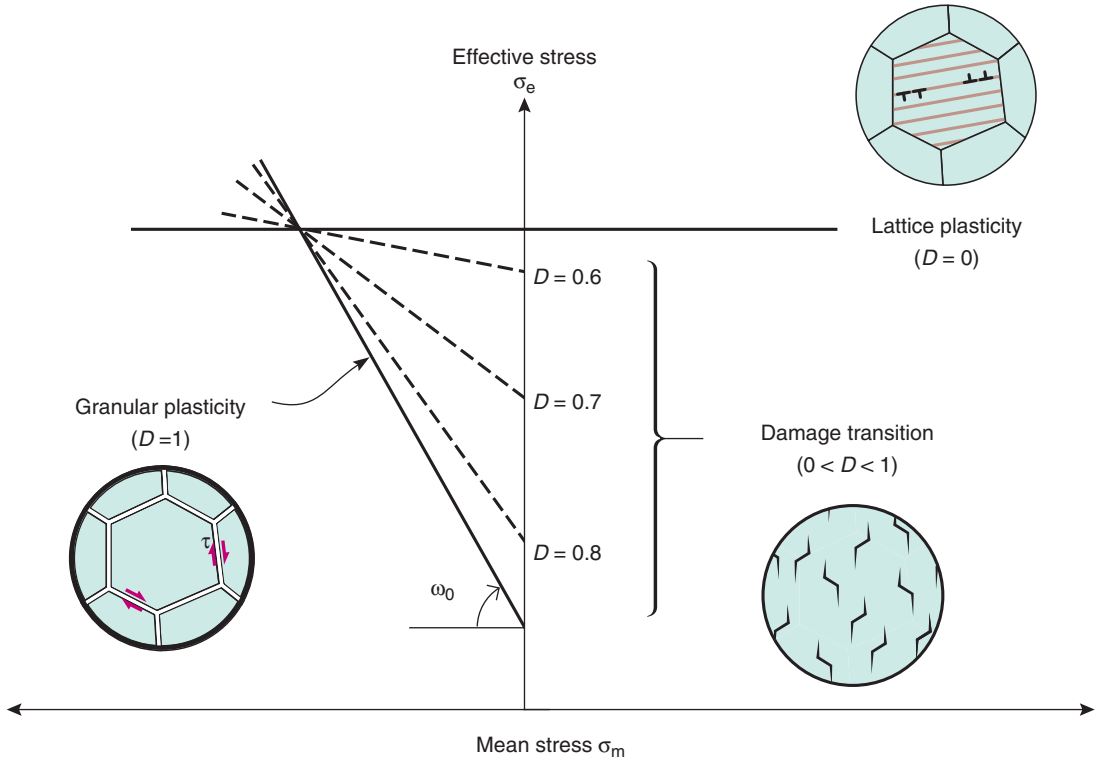

Fig. 2. Schematic of the yield surface transition from lattice to granular plasticity.

development of the microcracks is governed by the mode I stress intensity, K_I, at the tip of the wing cracks. In turn, K_I depends on the stress triaxiality, $\lambda \equiv \sigma_m/\sigma_e$, in accordance with three behavioral regimes (*I*, *II*, *III*) with four associated nonlinear functions of damage and friction (*A*, *B*, *C*, and *E*, defined in the Appendix A). In *Regime I* ($\lambda \leq -B/A$), the cracks are shut, with $K_I = 0$. In *Regime II*, frictional slip occurs along the initial flaw surfaces, with

$$K_I/\sqrt{\pi a} = A\sigma_m + B\sigma_e \tag{4}$$

In *Regime III*, $\lambda \geq AB/[C^2 - A^2]$, contact along the faces of the initial flaw is lost, where upon

$$K_I/\sqrt{\pi a} = (C^2\sigma_m^2 + E^2\sigma_e^2)^{1/2} \tag{5}$$

The crack growth rate, $\dot{\ell}$ is related to the stress intensity factor by

$$\dot{\ell} = \begin{cases} \min\left[\dot{\ell}_0 (K_I/K_{IC})^m, \sqrt{G/\rho_0}\right] & D < 1 \\ 0 & \text{otherwise} \end{cases} \tag{6}$$

where K_{IC} is the mode I (short-crack) fracture toughness, m is a rate exponent, and $\dot{\ell}_0$ the reference crack growth rate at $K_I = K_{IC}$. The crack speed is limited by the shear wave speed $\sqrt{G/\rho_0}$, where G and ρ_0 are the shear modulus and density of the intact ceramic, respectively. When $D \to 1$, the microcracks coalesce, causing $K_I \to \infty$ (in *Regimes II and III*), thus requiring that the microcracking model be supplanted by the ensuing model for granular plasticity. This is where the new model deviates from that originally proposed by Deshpande and Evans.[10]

(C) Granular Plasticity: The comminuted ceramic is modeled as a granular medium using a nonassociated, viscoplastic, Drucker–Prager type constitutive law, with an effective stress, $\hat{\sigma}$, defined as

$$\hat{\sigma} \equiv \frac{\sigma_e + (\tan\omega)\sigma_m}{1 - \tan\omega/3} \tag{7}$$

where ω is the friction angle. The factor in the denominator ensures that, under a uniaxial compressive stress σ, the effective stress $\hat{\sigma} \equiv |\sigma|$.

The effective stress is used to define an effective strain rate $\dot{\varepsilon}_c^g$, motivated by the following considerations. Under compressive hydrostatic stress states ($\sigma_m < 0$), the flow of the comminuted ceramic is expected to follow a Bagnold-type granular flow law,[14] wherein the effective stress for the medium scales with the square of the effective strain rate. This relation arises because the stresses generated in the medium at high-strain rates are not associated with interparticle friction but, rather, are due to repeated collisions between particles. During these collisions, both the momentum change per collision and the number of collisions per unit time are proportional to the strain rate, resulting in the quadratic scaling. In contrast, for tensile hydrostatic stress states ($\sigma_m > 0$), particle interactions are negligible, violating the assumptions that underpin Bagnold flow. These features suggest an overstress model of the form:

$$\frac{\dot{\varepsilon}_c^g}{\dot{\varepsilon}_s} = \begin{cases} \left(\dfrac{\hat{\sigma}}{\Sigma_c} - 1\right)^s & \hat{\sigma} > \Sigma_c \\ 0 & \text{otherwise} \end{cases} \tag{8a}$$

where Σ_c is the uniaxial compressive strength of the ceramic and $\dot{\varepsilon}_s$ a reference strain rate (specified subsequently in Section II*(2)*). Consistent with Bagnold scaling, the exponent is selected to be $s = 0.5$ when $\sigma_m \leq 0$: whereupon (8*a*) gives the Bagnold scaling $\dot{\varepsilon}_c^g \sim \sqrt{\hat{\sigma}}$ in the limit $\hat{\sigma} \gg \Sigma_c$. Conversely, when $\sigma_m > 0$, s needs to be large (typically $s = s_0 \geq 10$) to ensure that $\hat{\sigma}$ does not significantly exceed the uniaxial strength, Σ_c, thereby preventing the comminuted ceramic from attaining unreasonably high-tensile stresses. To ensure that the strain rate $\dot{\varepsilon}_c^g$ is continuous around $\sigma_m = 0$, a piecewise function for s is specified, with

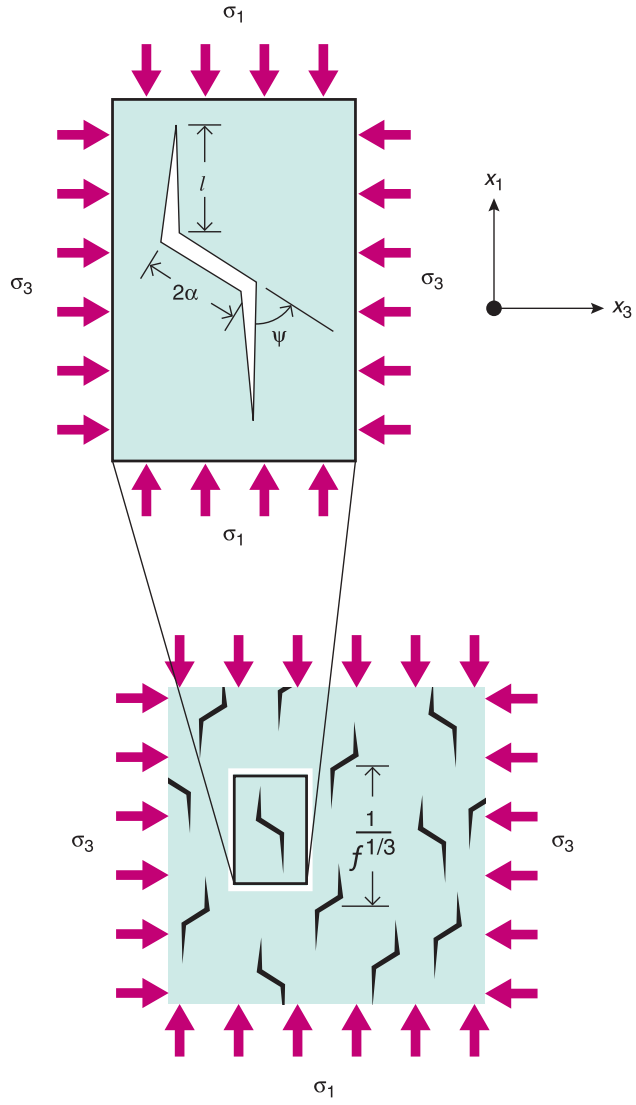

Fig. 3. Schematic of a microcracked solid containing an array of wing cracks.

the transition from $s = 0.5$ to s_0 occurring over the range $-\Sigma_c \le \sigma_m \le \Sigma_c$ and given by

$$s = \begin{cases} s_0 & \sigma_m \ge \Sigma_c \\ s_0 + \frac{1}{2}(s_0 - 0.5)\left(\frac{\sigma_m - \Sigma_c}{\Sigma_c}\right)^q & 0 \le \sigma_m < \Sigma_c \\ 0.5 + \frac{1}{2}(s_0 - 0.5)\left(\frac{\sigma_m + \Sigma_c}{\Sigma_c}\right)^q & -\Sigma_c \le \sigma_m < 0 \\ 0.5 & \text{otherwise} \end{cases} \tag{8b}$$

where the exponent q governs the transition rate.

To complete the characterization, a flow rule is specified. Experiments by Bagnold[14] and others suggest that, when deformation is governed by particle collisions, flow is nonassociated such that the flow potential is not determined by $\hat{\sigma}$. To ensure this generality, a flow surface G_g is defined as

$$G_g \equiv \begin{cases} \sigma_e + (\tan\delta)\sigma_m & \sigma_m < 0 \\ \sqrt{(\varepsilon\Sigma_t)^2 + \sigma_e^2} + \frac{\Sigma_c}{\Sigma_t}\sigma_m & \text{otherwise} \end{cases} \tag{9a}$$

where Σ_t is the hydrostatic tensile strength, given by setting $\hat{\sigma} = \Sigma_c$ and $\sigma_m/\sigma_e = 1/3$ in Eq. (7)

$$\Sigma_t \equiv \frac{\Sigma_c(1 - \tan\omega/3)}{\tan\omega} \tag{9b}$$

The quantity δ is the flow dilatation angle of the comminuted ceramic defined such that, when $\delta = 0$, the flow is volume conserving under compressive hydrostatic stress states. The parameter ε is a nondimensional regularization parameter (taken as 0.01) used to ensure that the flow is purely dilatational under hydrostatic tension. The granular strain rate follows from the flow surface G_g as

$$\dot{\varepsilon}_{ij}^g = \frac{\dot{\varepsilon}_e^g}{\varsigma}\frac{\partial G_g}{\partial \sigma_{ij}} \tag{10a}$$

where the normalization parameter is

$$\varsigma \equiv \begin{cases} \sqrt{\frac{3}{2} + \frac{1}{3}(\tan\delta)^2} & \sigma_m < 0 \\ \sqrt{\frac{(3/2)\sigma_e^2}{(\varepsilon\Sigma_t)^2 + \sigma_e^2} + \frac{1}{3}\left(\frac{\Sigma_c}{\Sigma_t}\right)^2} & \text{otherwise} \end{cases}. \tag{10b}$$

The factor ς is included in the flow rule so that

$$\left(\frac{1}{\varsigma}\frac{\partial G_g}{\partial \sigma_{ij}}\right)\left(\frac{1}{\varsigma}\frac{\partial G_g}{\partial \sigma_{ij}}\right) \equiv 1 \tag{11}$$

i.e., the magnitude of the effective granular plastic strain rate is set solely by $\dot{\varepsilon}_e^g$ with $\dot{\varepsilon}_e^g \equiv \sqrt{\dot{\varepsilon}_{ij}^g \dot{\varepsilon}_{ij}^g}$, while the direction of plastic straining is given by $\frac{\partial G_g}{\partial \sigma_{ij}}$.

(2) The Transition from Lattice to Granular Plasticity

Now that the basic models have been established, linkages must be provided. Namely, because the granular plasticity model is valid for all states of the comminuted ceramic (over the entire range $D_0 \le D \le 1$), evolution equations of the granular plasticity parameters from $D = D_0$ to $D = 1$ are required. These equations are specified through four parameters: (i) the uniaxial compressive strength Σ_c; (ii) the friction angle ω; (iii) the flow dilatation angle δ and (iv) a reference granular strain rate $\dot{\varepsilon}_s$. In its initial intact state (with $D = D_0$), the ceramic behaves as a von-Mises plastic material (with no contribution from granular plasticity). Accordingly, the granular plasticity parameters are chosen to ensure that, when $D = D_0$, the Drucker–Prager model reduces to the von-Mises model and that the granular strain rate is zero. The following evolution equations then ensue.

(i) *Uniaxial compressive strength* Σ_c. As D increases, Σ_c decreases from the plastic yield strength σ_0 to the fully comminuted strength σ_c, specified using

$$\Sigma_c = \sigma_0 - (\sigma_0 - \sigma_c)\left(\frac{D - D_0}{1 - D_0}\right)^q \tag{12}$$

The exponent q governs the transition rate with respect to D.

(ii) *The friction angle* ω. When the granular strength Σ_c is equal to the plastic yield strength σ_0, the friction angle $\omega = 0$. The angle increases with damage, reaching a value ω_0 upon complete comminution. Its evolution with the current material strength is specified by:

$$\tan\omega = \frac{(\sigma_0 - \Sigma_c)\tan\omega_0}{\sigma_0 - \sigma_c(1 - \tan\omega_0/3) - \Sigma_c\tan\omega_0/3} \tag{13a}$$

Thus, the granular yield surface evolves by pivoting about a coordinate in stress space defined by $\sigma_e = \sigma_0$ and

$$\sigma_m = \frac{\sigma_0 - \sigma_c}{\tan\omega_0} + \frac{\sigma_c}{3} \tag{13b}$$

This evolution is depicted in Fig. 2.

(iii) *The flow dilatation angle* δ. Because the intact ceramic behaves as an incompressible plastic medium, the flow dilatation angle should vary between $\delta = 0$ at $D = D_0$ to that for the fully

comminuted ceramic, δ_0, at $D = 1$. Thus, analogous to Eq. (12), the angle varies as

$$\delta = \delta_0 \left(\frac{D - D_0}{1 - D_0} \right)^q \tag{14}$$

(iv) *Reference granular strain rate* $\dot{\varepsilon}_s$. Granular straining does not occur in the undamaged ceramic. Thus $\dot{\varepsilon}_s$ is varied between $\dot{\varepsilon}_s = 0$ at $D = D_0$ to $\dot{\varepsilon}_{so}$ for the fully comminuted ceramic at $D = 1$, in accordance with:

$$\dot{\varepsilon}_s = \dot{\varepsilon}_{so} \left(\frac{D - D_0}{1 - D_0} \right)^q \tag{15}$$

It remains to estimate the reference strain rate $\dot{\varepsilon}_{so}$. The Bagnold[14] analysis suggests that the strength σ_c of the fully comminuted material scales as

$$\sigma_c \sim \left[\frac{e(1+e)\pi}{6} \left(\frac{\bar{\rho}^{1/3}}{1 - \bar{\rho}^{1/3}} \right)^2 \rho_0 d^2 \right] \dot{\varepsilon}_{so}^2 \tag{16}$$

where d is the particle size, e is the co-efficient of restitution between particles while the relative packing density $\bar{\rho}$ specifies the interparticle spacing. Given values of $\bar{\rho}$ and σ_c, Eq. (16) can be used to estimate $\dot{\varepsilon}_{so}$.

(3) The Overall Constitutive Model

The lattice and granular plasticity models are combined with elasticity to complete the overall model. The dynamic response is dominated by lattice plasticity and granular flow with negligible energy absorption involved in microcracking.[11] Moreover, the elastic strains are small compared to those for lattice plasticity and granular flow. Thus, unlike the model of Deshpande and Evans,[10] the elastic response upon microcracking is left unmodified, i.e. no stiffness reduction compared to the undamaged ceramic for all D. The total strain rate $\dot{\varepsilon}_{ij}$ is the sum of the contributions from elasticity and lattice and granular plasticity. Thus, the elastic strain rate is given by

$$\dot{\varepsilon}_{ij}^e = \dot{\varepsilon}_{ij} - (\dot{\varepsilon}_{ij}^{pl} + \dot{\varepsilon}_{ij}^g) \tag{17}$$

The deviatoric elastic response is specified by an isotropic Hooke's law, with strain rate

$$\dot{D}_{ij} = \dot{\varepsilon}_{ij}^e - \dot{\varepsilon}_{kk}^e \delta_{ij} \tag{18a}$$

and deviatoric stress rate $\dot{S}_{ij}$ related via

$$\dot{S}_{ij} = 2G\dot{D}_{ij} \tag{18b}$$

where G is the shear modulus.

Two alternate formulations are used for the pressure, providing the flexibility needed to examine the importance of shocks within the ceramic under high rates of loading. (i) The *linear formulation* uses the isotropic Hooke's law, with bulk modulus κ related to shear modulus G and Poisson's ratio ν by

$$\kappa = \frac{2G(1+2\nu)}{3(1-2\nu)} \tag{19a}$$

with pressure then related to the logarithmic volumetric elastic strain by

$$p \equiv -\frac{\sigma_{kk}}{3} = -\kappa \varepsilon_{kk}^e \tag{19b}$$

where $\varepsilon_{kk}^e = \int \dot{\varepsilon}_{kk}^e \mathrm{d}t$. (ii) In order to allow for shock formation at high pressures, an alternative formulation wherein pressure is specified by an equation of state can be used. The *Mie–Grüneisen equation of state* expresses the pressure in terms of the nominal volumetric elastic strain η and the internal energy per unit mass E_m. The internal energy is evaluated using the evolution equation

$$\frac{\partial(\rho E_m)}{\partial t} = \sigma_{ij}\dot{\varepsilon}_{ij} \tag{20a}$$

where ρ is the current density of the damaged ceramic, while the nominal compressive elastic strain is

$$\eta = 1 - \exp(\varepsilon_{kk}^e) \tag{20b}$$

These two state variables are related to the pressure by

$$p = \frac{\rho_0 c_0^2 \eta}{(1 - \vartheta\eta)^2} \left(1 - \frac{\Gamma_0 \eta}{2} \right) + \Gamma_0 \rho_0 E_m \tag{21}$$

where ρ_0 is the initial density of the ceramic, c_0 the initial p-wave speed ($\rho_0 c_0^2$ being equivalent to the elastic bulk modulus at small nominal strains), while Γ_0 and ϑ are dimensionless material constants measured from shock experiments. This equation predicts a linear shock velocity (u_s) versus particle velocity (u_p) relation of the form

$$u_s = c_0 + \vartheta u_p \tag{22}$$

In a finite element (FE) implementation, an artificial viscosity is included in Eq. (21) to enable the numerical solution to capture the development and propagation of the shock. Thus Eq. (21) is modified as

$$p = \frac{\rho_0 c_0^2 \eta}{(1 - s\eta)^2} \left(1 - \frac{\Gamma_0 \eta}{2} \right) + \Gamma_0 \rho_0 E_m + p_{bv} \tag{23}$$

where p_{bv} is the contribution to the pressure from the viscosity. Following von Neumann, a quadratic dependence of the viscous pressure on volumetric strain rate is typically employed:

$$p_{bv} = \begin{cases} 0 & \dot{\varepsilon}_{kk} \geq 0 \\ \rho_0 (b_1 L_e \dot{\varepsilon}_{kk})^2 & \text{otherwise} \end{cases} \tag{24}$$

where $b_1 \sim 1.2$ is the damping constant and L_e the characteristic length of the element in the FE mesh. We note in passing that an artifical shear viscosity is usually not required to stabilize the numerical calculations as both granular and lattice plasticity endow the material with a shear rate dependence.

With the deviatoric and mean stresses specified, the total stress σ_{ij} follows directly as

$$\sigma_{ij} = S_{ij} - p\delta_{ij} \tag{25}$$

(4) Choice of Material Parameters

In the subsequent section, the main features of the constitutive model are demonstrated through computations of various loading scenarios, with emphasis on effects of stress triaxiality. Except where otherwise noted, all computations use material parameters representative of alumina with a grain size $d = 3$ μm. These parameters have been carefully calibrated via a series of experiments reported in the companion paper Gamble *et al.*[15] The ceramic is elastically isotropic with Young's modulus $E = 405$ GPa, Poisson's ratio $\nu = 0.22$, density $\rho_0 = 3810$ kg/m^3, and fracture toughness $K_{IC} = 3$ MPa m$^{1/2}$. Based on a representative Vickers hardness, the yield strength and strain are taken as $\sigma_Y = 5.75$ GPa and $\varepsilon_Y = 0.002$, respectively, with $M = 0.1$ chosen to give a mildly strain hardening response.

The strain rate sensitivity parameters are chosen as $n = 34$, $\dot{\varepsilon}_0 = 10^{-3}$ s^{-1} and $\dot{\varepsilon}_t = 10^6$ s^{-1} while the crack growth parameters are taken to be $l_0 = 10$ mms^{-1} and $m = 30$. Following Ashby and Sammis,[16] the geometrical constants are taken as $\beta = 0.45$, $\alpha = 1/\sqrt{2}$ and $\gamma = 2.0$ (see Appendix A) with a friction coefficient $\mu = 0.75$. The assumed flaw size and spacing parameters are $g_2 = 6$ and $g_1 = 1/2$, which yield $f = 1.74 \times 10^5$ mm^{-3} and $D_0 = 8.57 \times 10^{-4}$. The granular plasticity parameters are: friction angle $\omega_0 = 70^\circ$, flow dilatation angle $\delta_0 = 0^\circ$, and uniaxial compressive strength of the comminuted ceramic $\sigma_c = 1$ MPa. The transition exponent is set as $q = 5$ while the granular rate sensitivity exponent in the hydrostatic tensile regime is chosen to be $s_0 = 10$. Taking $e = 1$ and $\bar{\rho} = 0.99$ in Eq. (16) gives the reference granular strain rate as $\dot{\varepsilon}_{so} = 2 \times 10^4$ s^{-1}. The pressure is specified using the linear (Hookean) formulation (i.e., shock effects as modeled by the Mie–Grüneisen equation of state are neglected).

III. Effects of Triaxiality on Intrinsic Material Response

The intrinsic stress versus strain response of the material was computed by integrating the constitutive equations detailed above for a total imposed strain rate of $\dot{\varepsilon}_e \equiv \sqrt{(2/3)\dot{\varepsilon}^d_{ij}\dot{\varepsilon}^d_{ij}} = 100$ s^{-1}, neglecting inertial or wave effects. The results are plotted in Fig. 4(a) for several selected values of stress triaxiality, representative of low ($\lambda = -0.1$) to high-confining pressure ($\lambda = -0.5$).

The predictions are qualitatively similar to those of the DE model.[10] For $\lambda = -0.1$ and $-1/3$ (uniaxial compression), the response is approximately linear elastic up to a peak stress, whereupon a sharp load drop occurs. The drop corresponds to a sudden increase in D from D_0 to unity. Thereafter, continued deformation in both cases occurs by granular plasticity at the much reduced stress value of σ_c. For higher levels of imposed pressure, characterized, for instance, by $\lambda = -0.5$, cracking does not occur and inelastic deformation occurs by lattice plasticity alone. The key difference between the behavior of the current model and the DE model is that, after the onset of damage, the DE model predicts a dilatant response, dictated by the extent of crack opening. By contrast, the addition of granular plasticity in the current formulation means that the postcracking dilatation is controlled independently: in the present computations, with the selection $\delta_0 = 0^\circ$, no volume change occurs under compressive hydrostatic stresses.

Another feature of both the original DE model and the current one is that, once fully comminuted, the material can sustain considerable stresses provided sufficiently high-confining pressures are imposed during subsequent loading. This feature is illustrated in Fig. 4(b). Here the loading occurs in two steps. In the first, the ceramic is loaded at a strain rate $\dot{\varepsilon}_e = 100$ s^{-1} while the triaxiality is fixed at $\lambda = -1/3$ (as in Fig. 4(a)). Following the load drop at $\sigma_e \approx 6$ GPa, continued straining (up to $\varepsilon_e = 0.012$) occurs at a negligible stress. In the second step, the confining pressure is increased, to $\lambda = -0.6$, and deformation continued at $\dot{\varepsilon}_e = 100$ s^{-1}. Under these conditions, granular plasticity is suspended and the ceramic is able to sustain high stresses and deform by lattice plasticity within the comminuted particles.

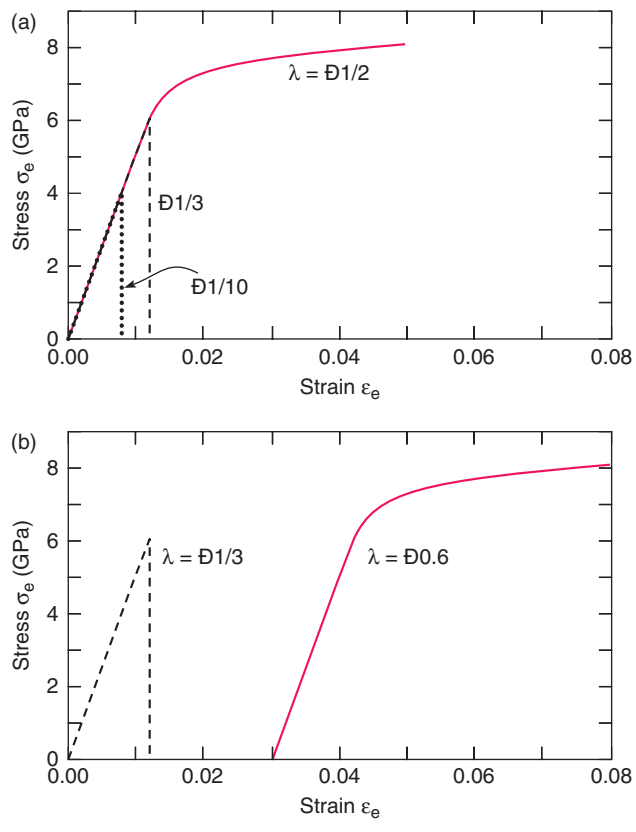

Fig. 4. (a) Effects of triaxiality on the predicted stress/strain response of alumina with reference properties at a strain rate of 100 s^{-1}. (b) Illustrative example showing effects of a change in stress triaxiality, from $-1/3$ to -0.6, during deformation on the flow response of alumina.

IV. Dynamic Cavity Expansion

The dynamic elasto-plastic field induced by a pressurized spherical cavity expanding in an infinite medium is widely used as a protocol for ascertaining the key phenomena accompanying penetration. An extensive review of early work has been given by Hopkins[17] with emphasis on metals characterized by Mises plasticity. More recent interest in penetration into concrete and other geomaterials has instigated investigations of dynamic qcavity expansion in pressure-sensitive solids described by Mohr–Coloumb or Drucker–Prager constitutive laws.[18–20] More recently, analogous approaches have been used for ceramic targets.[21–22] However, in contrast to the present formulation, the ceramic models used in the aforementioned studies do not differentiate explicitly between lattice and granular plasticity. When the two are indeed decoupled from one another in the constitutive law, the computations of dynamic cavity expansion reveal important interactions between the two deformation mechanisms. This feature is highlighted here.

(1) Boundary Value Problem

A spherical cavity of initial radius a_0 in an infinite medium is pressurized by a constant and spatially uniform pressure p. Specifically, the pressure is zero at time $t = 0^-$ and equal to p_0 at $t \geq 0$ (Fig. 5). Neglecting symmetry-breaking modes of deformation, the active components of the Cauchy stress are the radial stress σ_r and the hoop stresses $\sigma_\theta = \sigma_\phi$, and the radial

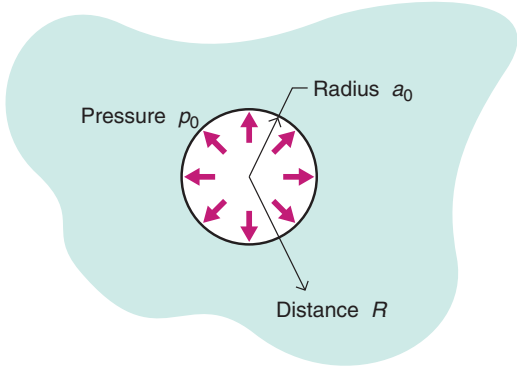

Fig. 5. Sketch of the boundary value problem for the expansion of a spherical cavity in an infinite medium.

equation of motion is given by

$$\frac{\partial}{\partial r}(r^2\sigma_r) - 2r\sigma_\theta = \rho\ddot{u}r^2 \tag{26}$$

where r denotes the radial position of a material point in the current configuration, u is the radial displacement of that point, the overdot denotes differentiation with respect to time, and ρ is the material density in the current configuration. Equation (26) is solved using an updated Lagrangian scheme, detailed in Deshpande and Evans.[10] In the FE calculations, the outer radius of the medium being analyzed is taken to be sufficiently large so as to ensure that the elastic wave does not reach the outer boundary over the time-span of the calculations reported here, thereby simulating an infinite medium. Unless otherwise specified, the computations use the property values for alumina (summarized in Section II*(4)*). The focus of subsequent numerical results and discussion is on the early time response, wherein dynamic effects dominate. For the expansion of a spherical cavity in an infinite *elastic* medium, Hopkins[17] has shown that the stress distributions near the vicinity of the cavity are well approximated by the corresponding quasi-static result at times $\bar{t} \equiv c_e t/a_0 > 4$, where c_e is the p-wave speed. Thus, all results presented here are for times $\bar{t} < 4$.

(2) Effect of Pressure

The predicted temporal variation of the radial displacement U/a_0 of the cavity surface is plotted against time $\bar{t}$ in Fig. 6 for three levels of the cavity pressure. The cavity displacement increases approximately linearly with time for the three pressure levels considered here. We proceed to investigate in further detail the cases in which $p_0 = 12$ and 24 GPa.

First consider the case where $p_0 = 12$ GPa. The spatial distributions of damage D, effective lattice plastic strain ε_e^{pl} and effective granular plastic strain ε_e^{g} are plotted in Fig. 7(a) at three select times. Note that ε_e^{pl} and ε_e^{g} are the time integrals of the strain rates given by Eqs. (1) and (8*a*), respectively. The distributions are plotted as a function of R/a_0, where R is the radial coordinate in the undeformed configuration. Full comminution of the ceramic (i.e., $D = 1$) first occurs at a finite distance from the cavity surface, viz. at $R/a_0 \approx 1.5$. The damage zone then expands radially inwards while simultaneously expanding outwards. However, while the damage zone continues to expand outwards for the duration of the computations, the progression of the damage zone toward the surface to the cavity halts at time $\bar{t} \approx 1.4$ when the inner boundary of the damage zone reaches $R/a_0 \approx 1.1$, i.e., the damage zone does not extend up to the cavity surface. We shall show subsequently that this feature is due to the fact that the large lattice plastic strains near the cavity surface reduce the stress triaxiality and thereby reduce the propensity for microcracking. The spatial distributions of ε_e^{pl} included in Fig. 7(a) show that, for $\bar{t} > 1.4$, the lattice plastic strain rises sharply for $R/a_0 < 1.1$, i.e., the region over which damage does not occur. Correspondingly, the distribution of granular plastic strains clearly show that significant granular plasticity only occurs over the region where $D = 1$. Note that the total inelastic strains (i.e., lattice plus granular plastic strains) are continuous across the boundary of the damage zone near the surface of the cavity; while ε_e^{g} drops to zero across the boundary where the damage variable transitions from $D = 1$ to $D = D_o$, ε_e^{pl} rises sharply in order to keep the total inelastic strain approximately continuous.

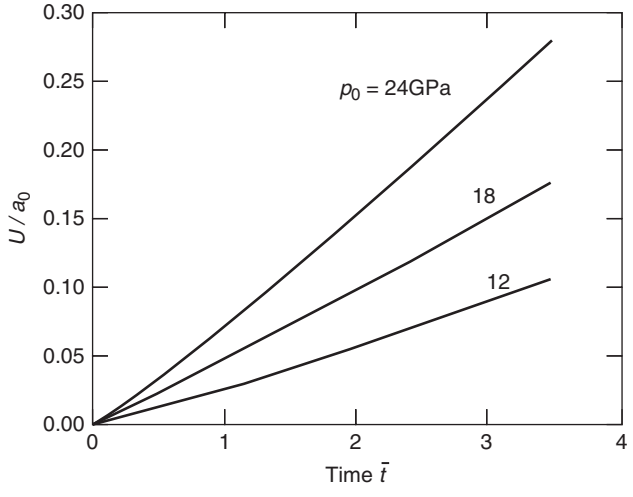

Fig. 6. The evolution of the radial displacement of the cavity surface with time. Results are for alumina with reference properties.

At the higher applied cavity pressure of $p_0 = 24$ GPa, the qualitative picture discussed above remains unchanged. However, the higher pressure means that the stress triaxiality near the cavity surface is further reduced and hence microcracking initiates even further away from the cavity surface at $R/a_0 \approx 2.2$ and expands *only* away from the cavity surface, where the stress triaxiality increases. The discontinuity in the value of ε_e^{pl} across the damage zone interface near the surface of the cavity is now more obvious. However, similar to the $p_0 = 12$ GPa case, the total inelastic strains are approximately continuous across this interface, with granular plasticity inside the damage zone replaced by lattice plasticity.

Insights into the effects of lattice plasticity on stress triaxiality (which in turn affect microcracking) are gleaned from computations in which the damage is artificially suppressed, by setting $K_{IC} = \infty$. The results are plotted in Fig. 8 for three times and three values of yield strength, selected such that $p_0/\sigma_Y = 1.71$, 1.5, and 0 when $p_0 = 24$ GPa. For the purely elastic case ($p_0/\sigma_Y = 0$), the triaxiality is at its lowest (most negative) at the elastic wave front (as noted by Hopkins[17]). Thus, absent lattice plasticity, damage initiates at the cavity surface, where both the stresses and the stress triaxiality are greatest, and propagates radially outward, trailing the elastic wave front. When lattice plasticity is activated, as in the cases of $p_0/\sigma_Y = 1.71$ and 1.5, plasticity initiates on the cavity surface, where the deviatoric stress is highest, and subsequently spreads radially outward. This plasticity results in a reduction in the stress triaxiality in the plastic zone, as evident upon comparison of the results for $p_0/\sigma_Y = 1.71$ and 1.5 with those of the elastic case. The magnitude of this effect increases with increasing plastic strain. Moving radially outward from the cavity surface, the plastic strain diminishes and hence its effect on stress triaxiality decreases. Eventually, the triaxiality reaches the value corresponding to the elastic case at the elastic/plastic interface. Because of the opposing effects of elastic wave propagation and plasticity on stress triaxiality—the elastic wave reducing triaxiality with increasing R/a_0 and the near-surface plasticity reducing triaxiality as $R/a_0 \to 1$—the triaxiality attains a *maximum value at a finite distance* away from the cavity surface. For cases where damage is activated (such as that shown in Fig. 7), damage initiates at or near this location and then spreads radially both inward and outward. A corollary of the results presented in Fig. 8 is that the stress triaxiality decreases with increasing values of p_0/σ_Y, due to the increased levels of lattice plasticity. This is evident from comparisons of the results for $p_0/\sigma_Y = 1.71$ and 1.5 in Fig. 8. The reductions in the stress triaxiality for higher values of p_0/σ_Y result in damage initiating further away from the cavity surface as observed in Fig. 7(b).

(3) The Interplay Between Plasticity and Damage

The results in the preceding section demonstrate the interplay between lattice plasticity and stress triaxiality. Its connection to damage development and cavity expansion emerges from a series of computations for a cavity pressure $p_0 = 12$ GPa and three values of yield strength σ_Y (all other material properties being kept fixed at their reference values, including the finite fracture toughness). The variation in the displacement of the cavity surface U/a_0 with time $\bar{t}$ for each of these cases is plotted in

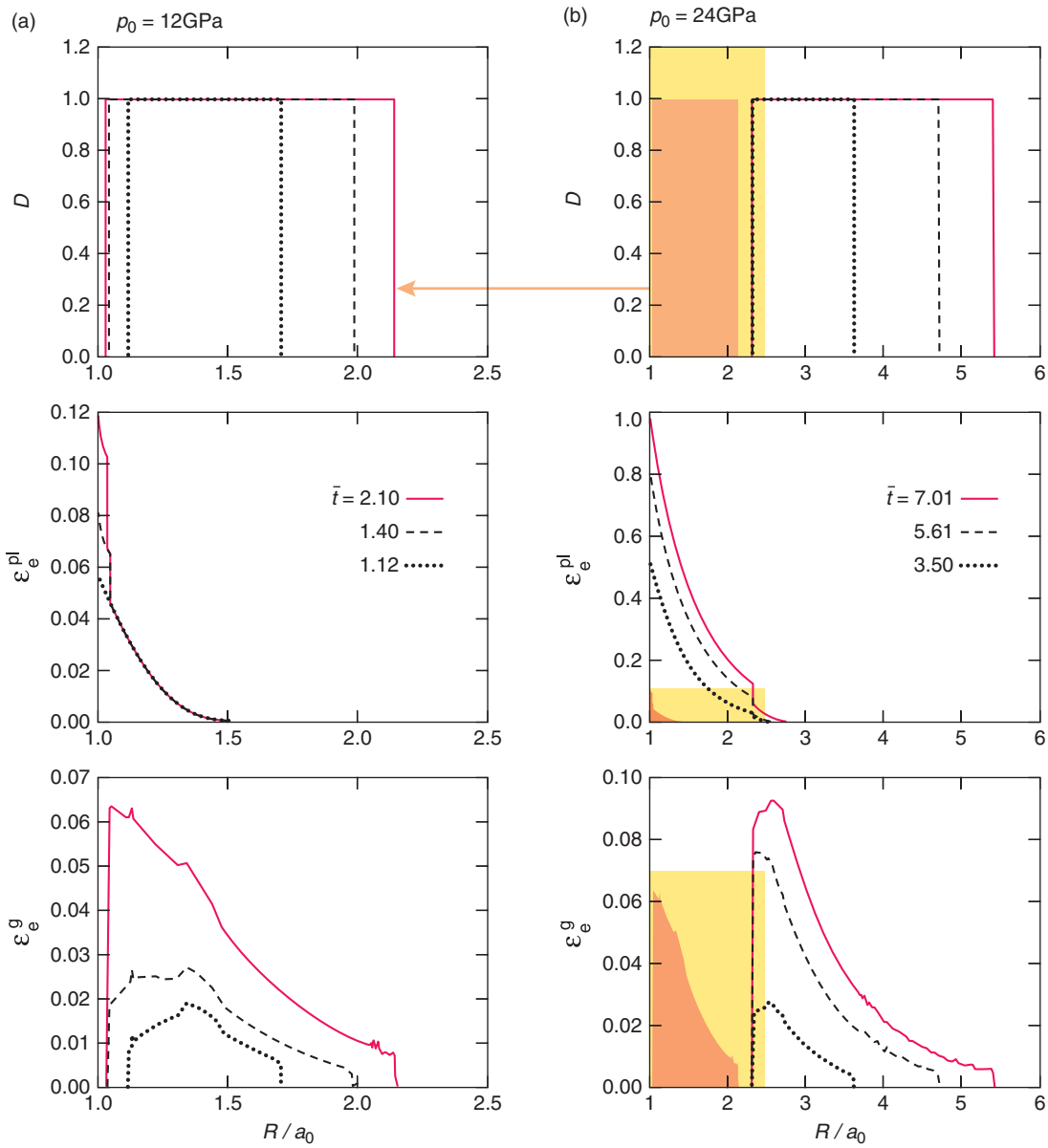

Fig. 7. Spatial distributions of damage D, effective lattice plastic strain ε_e^{pl} and effective granular plastic strain ε_e^{g} for applied cavity pressures, p_0, of (a) 12 GPa and (b) 24 GPa. Results are shown for alumina with reference properties at three select times $\bar{t}$.

Fig. 9(a). Interestingly, the cavity expansions are approximately equal for the $\sigma_Y = 5$ and 9 GPa cases (indeed, slightly lower for $\sigma_Y = 5$ GPa) but significantly higher for $\sigma_Y = 3$ GPa. In order to parameterise this information we plot the cavity displacement U_c/a_0 at a time $\bar{t} = 3$ against yield strength σ_Y in Fig. 9(b) for cavity pressures $p_0 = 12$ and 24 GPa. Three regimes emerge: one is dominated by damage, at high values of σ_Y, wherein U_c/a_0 is independent of σ_Y; a second dominated by lattice plasticity, wherein U_c/a_0 increases with decreasing σ_Y; and an intermediate regime in which lattice plasticity and damage occur simultaneously. Thus, there exists a critical value of σ_Y above which U_c does not decrease any further. This clearly shows that increasing the yield strength of the ceramic indefinitely will not bring any further performance benefits as the response becomes dominated by the microcracking deformation mode. However, the critical value of σ_Y increases with increasing applied pressure; for the parameters considered here, the critical yield strength increases from $\sigma_Y \approx 5$ to 8 GPa as p_0 increases from 12 to 24 GPa.

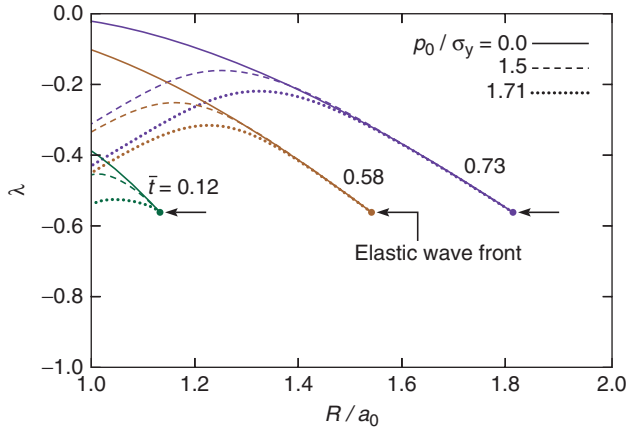

Fig. 8. Evolution of stress triaxiality associated with dynamic spherical cavity expansion in an elastic–plastic (nondamaging) alumina.

V. Indentation

The fidelity of the model has been assessed in two companion studies (B. Compton *et al.*, unpublished data).[15] Here we highlight some of their results in order to illustrate the applicability of the model. All tests were performed on an armor-grade

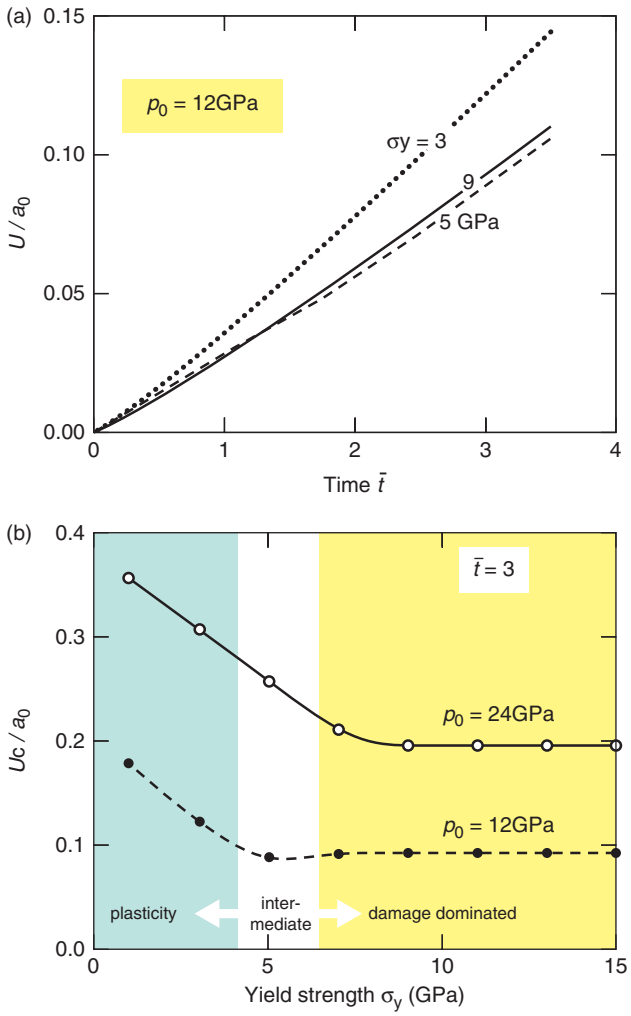

Fig. 9. (a) The evolution of radial displacement of the cavity surface with time for an applied cavity pressure $p_0 = 12$ GPa. (b) Effects of yield strength and pressure on the radial cavity displacement U_c at time $\bar{t} = 3$.

alumina (Corbit 98, produced by Industri Bitossi, Sovigliana vinci, Florence, Italy) with an average grain size $d = 3$ μm. It consists of 98% alumina and minor amounts of a glassy phase, the latter being situated predominantly at triple grain junctions. Details of the properties of this material and the model parameters (listed in Section II*(4)*) as well as the procedures used to obtain their values are in.[15]

(1) Quasi-static Indentation

The quasi-static penetration resistance was probed using a spheroconical diamond indenter with a 200 μm tip radius and 120° cone angle, mounted on a conventional servo-hydraulic mechanical test system.[15] Displacements were measured with submicrometer accuracy using a one-armed extensometer positioned on the alumina surface. Additionally, corrections for machine compliance and elastic (Hertzian) deformation of the indenter were used to remove displacements external to the indentation site. Corresponding FE computations were performed using the current model and the original DE model. (The parameter set of the DE model is a subset of the current model, i.e., all parameters of the current model expect those associated with granular plasticity. To make a fair comparison between the current and DE models we use the values parameters listed in Section II*(4)* in the calculations with the DE model as well.)

Figure 10 shows a comparison between predictions and measurements of both the load–displacement response and the damage immediately under the indenter at an applied load of 200 N. The current model is shown to accurately predict both the extent of the damage immediately under the indenter and the load versus penetration response. By contrast, the DE model predicts significantly greater damage and unrealistically large surface uplift around the indent periphery. This large damage manifests as large inelastic displacements during loading and hence the DE model also does not predict the measured load versus penetration response with an adequate level of accuracy. These discrepancies of the DE model are a consequence of the elastic dilatation associated with the cracks but not associated with granular plasticity.

(2) Dynamic Indentation

Constrained alumina tiles, each 50 mm × 50 mm × 12 mm thick, were impacted by 7.14 mm diameter steel spheres at velocities in the range 300–800 ms^{-1} (B. Compton *et al.*, unpublished data).

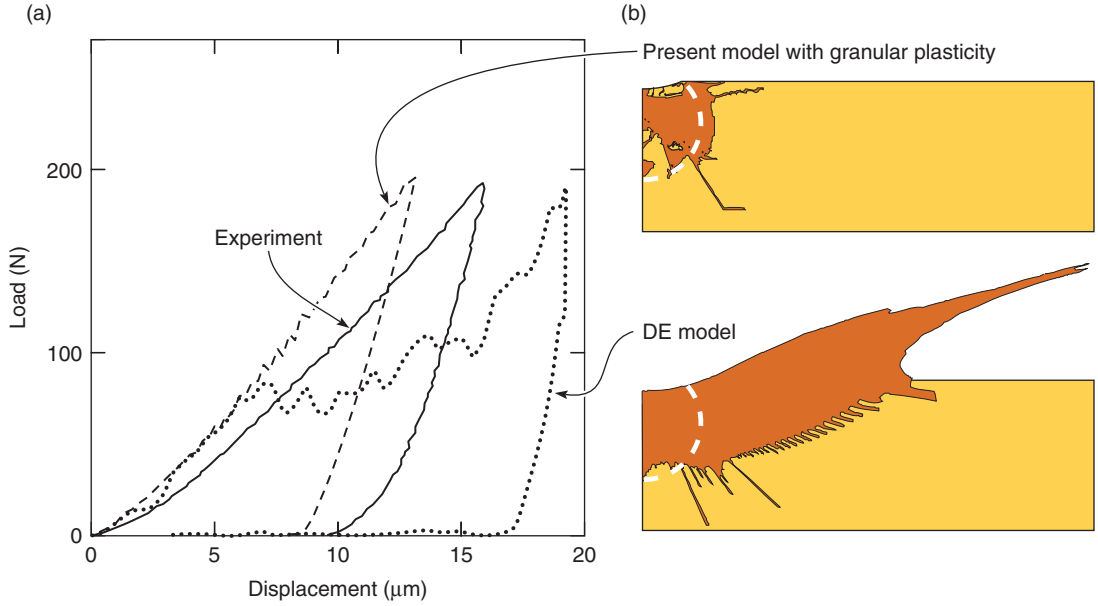

Fig. 10. (a) Comparisons between predicted and measured quasi-static indentation responses. (b) Corresponding subsurface damage at an applied load of 200 N. Predictions are shown for both the current and the DE models with the area shaded dark corresponding to fully microcracked ceramic. The dashed lines indicate the extent of the observed commutated zone (Adapted from[15]).

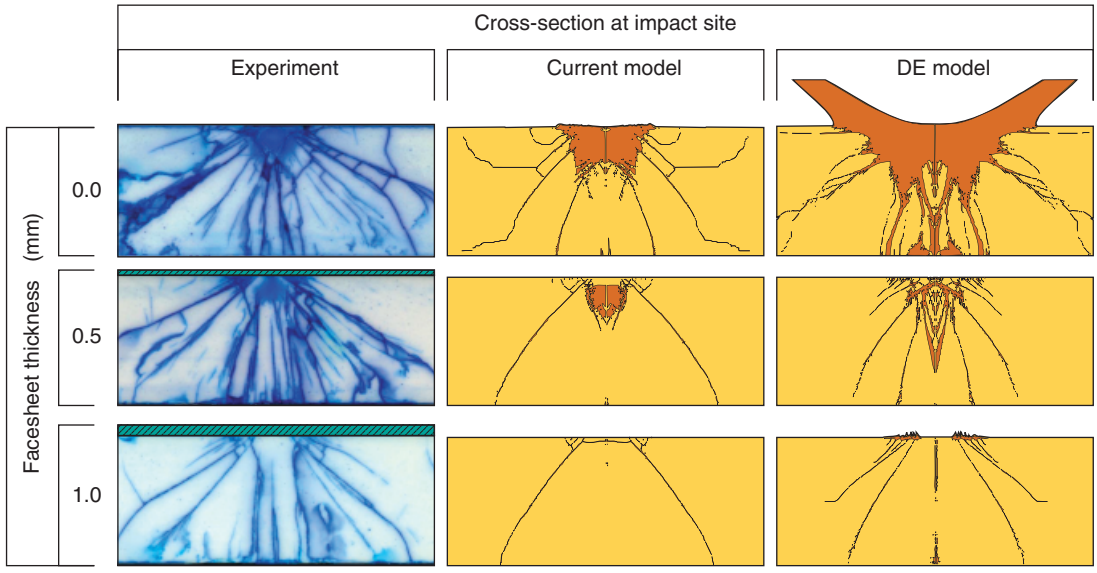

Fig. 11. Comparisons between predicted and measured subsurface damage in alumina resulting from impact of a 304 stainless-steel (SS) sphere at an incident velocity of 750 ms^{-1}. The dark shaded regions are fully damaged whereas the light shaded regions are undamaged. Predictions are shown for both the current and the DE models. Three cases are considered: no face-sheet, 0.5-mm-thick 304 SS face-sheet and 1-mm-thick 304 SS face-sheet.

Three situations were considered: (i) tiles with no face sheet; (ii) tiles with a 0.5 mm thick 304 stainless-steel face sheet; and (iii) tiles with a 1-mm-thick 304 stainless-steel face sheet. After the tests, the tiles were stained with a blue dye and impregnated with an epoxy resin in order to contain the comminuted ceramic. They were then sectioned in half in order to reveal the damage pattern directly beneath the impact site. Comparisons between the observations and the predictions (from both current and original DE models) for an impact velocity 750 ms^{-1} are presented in Fig. 11. The current model captures the observations for the three scenarios of present interest with reasonable fidelity, including the observation that the extent of damage is significantly reduced by the presence of the steel face sheets. By contrast, in line with the quasi-static indentation simulations, the DE model overestimates the damage significantly in all cases.

VI. Limitations of the Model

The micromechanical model for ceramics presented in this study has some inherent limitations that fall into two catagories: (i) limitations related to microstructural assumptions and (ii) limitations related to the neglecting of the statistical aspects of ceramic failure. Here we briefly discuss these limitations.

Three inelastic mechanisms have been accounted for in the approach presented here, viz. microcracking from preexisting flaws presumed to be present at grain boundaries, lattice plasticity and granular plasticity. Cracking in polycrystalline ceramics is however known to occur from numerous other sources of heterogeneities such as inclusions and voids,[23] glass present at grain boundaries[24] and surface flaws. The modeling framework presented here is sufficiently general that these mechanisms can be included in the constitutive model, albeit at the cost of greater complexity and additional material parameters that will inevitably require calibration. We thus expect to include these additional mechanisms as additional experimental data that suggests the need to incorporate these mechanisms becomes available.

It is well known that the failure strength of ceramics is both statistical in nature and size dependent. This is often well represented by the Weibull distribution.[25] The statistical effects give rise to the well-known observation that nominally identical ceramic specimens have different mechanical properties including sometime markedly different ballistic responses. To account for these statistical variations, Leavy *et al.*[26] included uncertainty into a deterministic model such as the Johnson and Holmquist[5] model. This enabled them to not only capture the observed failure patterns in a Brazilian test but including a distribution of strengths also significantly alleviated the mesh dependency problems inherent in these ceramic models that are based on a damage mechanics approach. Inclusion of uncertainty into the present model is a necessary next step in developing a predictive ceramic model for armor applications.

VII. Conclusions

A unified model for the dynamic inelastic response of ceramics under compressive stress states has been developed. It incorporates three inelastic deformation mechanisms: (i) lattice plasticity due to dislocation glide or twinning; (ii) microcrack extension; and (iii) granular flow of densely packed comminuted particles. In addition to analytical descriptions of each of these mechanisms, prescriptions have been provided for their implementation into a FE code as well as schemes for transitioning between mechanisms.

The utility of the code in addressing issues related to deep penetration has been demonstrated through a series of calculations of dynamic cavity expansion in an infinite medium subject to a fixed internal pressure p. The results reveal two limiting behavioral regimes: one dictated by lattice plasticity and another by granular plasticity. The competition between these two deformation mechanisms along with the interplay between plasticity and stress triaxiality lead to an optimal value of yield strength at which the cavity expansion rate is minimized. This result suggests that, once the damage and fracture parameters are specified, an optimal yield strength exists for superior penetration resistance at a prescribed pressure. It remains to be established whether this effect can be exploited in designing ceramics to resist penetration over a targeted range of loadings.

Granular plasticity proves to be an essential ingredient in the constitutive law, as demonstrated by the quasi-static and dynamic indentation studies. When neglected (as in the original DE model), the spatial extent of damage and the magnitude of the strains are strongly overpredicted. Nevertheless, the model fails to capture all features in the indentation response. Most notably, the formation of lateral subsurface cracks during the unloading phase of indentation cannot be predicted. To capture this feature along with the ensuing spallation that commonly accompanies indentation, the model would need to be expanded to include a fracture mechanics-based component for modeling "macro" rather than "micro" cracking.

Appendix A: Summary of Microcrack Growth Coefficients

The coefficients used in Section II(1) are defined as follows. The parameters A and B are given as

$$A \equiv c_1(c_2A_3 - c_2A_1 + c_3) \tag{A-1}$$

and

$$B \equiv \frac{c_1}{\sqrt{3}}(c_2A_3 + c_2A_1 + c_3) \tag{A-2}$$

where

$$c_1 = \frac{1}{\frac{\pi^2}{2^{3/4}}\left[\left(\frac{D}{D_0}\right)^{1/3} - 1 + \beta\sqrt{2}\right]^{3/2}} \tag{A-3}$$

$$c_2 = 1 + 2\left[\left(\frac{D}{D_0}\right)^{1/3} - 1\right]^2\left(\frac{D_0^{2/3}}{1 - D^{2/3}}\right) \tag{A-4}$$

and

$$c_3 = \pi^2\left[\left(\frac{D}{D_0}\right)^{1/3} - 1\right]^2 \tag{A-5}$$

while

$$A_1 = \pi\sqrt{\frac{\beta}{3}}[(1 + \mu^2)^{1/2} - \mu] \tag{A-6}$$

and

$$A_3 = A_1\left\{\frac{(1 + \mu^2)^{1/2} + \mu}{(1 + \mu^2)^{1/2} - \mu}\right\} \tag{A-7}$$

Here β is a coefficient introduced by Ashby and Sammis[16] to convert exact two-dimensional solutions to three-dimensional stress states. The coefficients E and C are defined as

$$E^2 = \frac{B^2C^2}{C^2 - A^2} \tag{A-8}$$

and

$$C \equiv A + \gamma\sqrt{\frac{1}{\sqrt{2}}\left(\frac{D}{D_0}\right)^{1/3}} \tag{A-9}$$

with γ a constant used to match tensile data.

Acknowledgments

E. A. G. was supported by a National Defense Science and Engineering Fellowship. V. S. D. acknowledges ONR for support via award no. N00014-09-1-0573.

References

[1]A. M. Rajendran and D. J. Grove, "Modeling the Shock Response of Silicon Carbide, Boron Carbide and Titanium Diboride," *Int. J. Impact Eng.*, **18**, 611–31 (1996).
[2]G. T. Camacho and M. Ortiz, "Computational Modeling of Impact Damage in Brittle Materials," *Int. J. Solids Struct.*, **33**, 2899–938 (1996).
[3]P. J. Hazell and M. J. Iremonger, "Crack Softening Damage Model for Ceramic Impact and its Application with in a Hydrocode," *J. Appl. Phys.*, **82**, 1088–92 (1997).
[4]H. D. Espinosa, P. D. Zavattieri, and S. K. Dwivedi, "A Finite Deformation Continuum/Discrete Model for the Description of Fragmentation and Damage in Brittle Materials," *J. Mech. Phys. Solids*, **46**, 1909–42 (1998).
[5]G. R. Johnson and T. J. Holmquist, "Response of Boron Carbide Subjected to Large Strains, High Strain Rates, and High Pressures," *J. Appl. Phys.*, **85**, 8060–73 (1999).
[6]C. H. M. Simha, S. J. Bless, and A. Bedford, "Computational Modeling of the Penetration Response of a High-Purity Ceramic," *Int. J. Impact Eng.*, **27**, 65–861 (2002).
[7]D. C. Drucker and W. Prager, "Soil Mechanics and Plastic Analysis or Limit Design," *Quart. Appl. Math.*, **10**, 157–65 (1952).
[8]G. R. Johnson and W. H. Cook, "Fracture Characteristics of Three Metals Subjected to Various Strains, Strain Tatesm Temperatures and Pressures," *Eng. Fract. Mech.*, **21**, 31–48 (1985).
[9]D. W. Templeton, T. J. Holmquist, H. W. Meyer, D. J. Grove, and B. Leavy, "A comparison of ceramic material models"; pp. 299–308 in *Proceedings of the Ceramic Armor by Design Symposium*, Pacific Rim IV International Conference on Advanced Glass and Ceramics, Wailea, Maui, Hawaii, 2001.
[10]V. S. Deshpande and A. G. Evans, "Inelastic Deformation and Energy Dissipation in Ceramics: A Mechanism-Based Dynamic Constitutive Model," *J. Mech. Phys. Solids*, **56**, 3077–100 (2008).
[11]Z. Wei, V. S. Deshpande, and A. G. Evans, "The Influence of Material Properties and Confinement on the Dynamic Penetration of Alumina by Hard Spheres," *J. Appl. Mech.*, **76**, 051305, 8pp (2009).
[12]Z. Wei, A. G. Evans, and V. S. Deshpande, "Mechanisms and Mechanics Governing the Indentation of Polycrystalline Alumina," *J. Am. Ceram. Soc.*, **91**, 2987–96 (2008).
[13]H. J. Frost and M. F. Ashby, *Deformation Mechanism Maps*. Pergamon Press, Oxford, 1982.
[14]R. A. Bagnold, "Experiments on a Gravity-Free Dispersion of Large Solid Particles in a Newtonian Fluid Under Shear," *Proc. R. Soc. Lond.*, **A225**, 49–63 (1954).
[15]E. A. Gamble, B. Compton, V. S. Deshpande, A. G. Evans, and F. W. Zok, "Penetration resistance of an armor ceramic: I- Quasi-static loading," *J. Am. Ceram. Soc.*, (2010) (this issue).
[16]M. F. Ashby and C. G. Sammis, "The Damage Mechanics of Brittle Solids in Compression," *Pure Appl. Geophys.*, **133**, 489–521 (1990).
[17]H. G. Hopkins, "Dynamic Expansion of Spherical Cavities in Metal"; pp. 85–164 in *Progress in Solid Mechanics*, Vol. 1, Edited by I. N. Sneddon, and R. Hill. North-Holland, Amsterdam, 1960.
[18]M. J. Forrestal, D. Y. Tzou, E. Askari, and D. B. Longcope, "Penetration into Ductile Metal Targets with Rigid Spherical-Nose Rods," *Int. J. Impact Eng.*, **16**, 699–710 (1995).
[19]R. W. Macek and T. A. Duffey, "Finite Cavity Expansion Method for Near-Surface Effects and Layering During Earth Penetration," *Int. J. Impact Eng.*, **24**, 239–58 (2000).
[20]D. Durban and R. Masri, "Dynamic Spherical Cavity Expansion in a Pressure Sensitive Elastoplastic Medium," *Int. J. Solids Struct.*, **41**, 5697–716 (2004).
[21]S. Satapathy, "Dynamic Spherical Cavity Expansion in Brittle Ceramics," *Int. J. Solids Struct.*, **38**, 5833–45 (2001).
[22]J. D. Walker, "Analytic model for penetration of thick ceramic targets"; pp. 337–48 in *Proceedings of the ceramic armor by design symposium*, Pacific Rim IV International Conference on Advanced Glass and Ceramics, Wailea, Maui, Hawaii, 2001.
[23]C. G. Sammis and M. F. Ashby, "The Failure of Brittle Porous Solids Under Compressive Stress States," *Acta Metall.*, **34**, 511–26 (1986).
[24]D. R. Clarke, "Grain Boundaries in Polycrystalline Ceramics," *Annu. Rev. Mater. Sci.*, **17**, 57–74 (1987).
[25]W. Weibull, "A Statistical Distribution Function of Wide Applicability," *J. Appl. Mech.*, **18**, 293–7 (1951).
[26]R. B. Leavy, R. M. Brannon, and O. E. Strack, "The Use of Sphere Indentation Experiments to Characterize Ceramic Damage Models," *Appl. Ceram. Technol.*, **7**, 606–15 (2010). □